

SHORT REPORT

Correlative super-resolution fluorescence and electron microscopy of the nuclear pore complex with molecular resolution

Anna Löschberger¹, Christian Franke¹, Georg Krohne², Sebastian van de Linde¹ and Markus Sauer^{1,*}

ABSTRACT

Here, we combine super-resolution fluorescence localization microscopy with scanning electron microscopy to map the position of proteins of nuclear pore complexes in isolated *Xenopus laevis* oocyte nuclear envelopes with molecular resolution in both imaging modes. We use the periodic molecular structure of the nuclear pore complex to superimpose direct stochastic optical reconstruction microscopy images with a precision of <20 nm on electron micrographs. The correlative images demonstrate quantitative molecular labeling and localization of nuclear pore complex proteins by standard immunocytochemistry with primary and secondary antibodies and reveal that the nuclear pore complex is composed of eight gp210 (also known as NUP210) protein homodimers. In addition, we find subpopulations of nuclear pore complexes with ninefold symmetry, which are found occasionally among the more typical eightfold symmetrical structures.

KEY WORDS: Correlative electron and super-resolution fluorescence microscopy, Nuclear pore complex, dSTORM, Localization microscopy, Quantification

INTRODUCTION

Electron microscopy (EM) and electron tomography have been extensively used to elucidate cellular ultrastructure and architecture of large multiprotein complexes. An impressive example of the resolution power of these methods is the determination of the three-dimensional (3D) structure of the nuclear pore complex (NPC), a gigantic molecular machine assembled from ~30 different nuclear proteins with a molecular mass of over 100 MDa, with a resolution of a few nanometers (Beck et al., 2007; Maimon et al., 2012). However, conventional fixation and staining protocols for EM and electron tomography are optimized to provide optimal preservation of cellular ultrastructure and not to provide specific molecular labeling. Immunolabeling EM with gold-conjugated antibodies can reveal localizations of cellular components with nanometer resolution but is limited by the quality of fixation and the inaccessibility of antigens, and it can obscure structural details beneath it. Even under optimized conditions (i.e. with the availability of high-affinity antibodies and mild fixation and staining protocols) only a subset of target molecules is likely to be successfully detected

(Morphew, 2007). Hence, the determination of the molecular composition of large biological complexes, such as the NPC, remains challenging.

Correlative light and electron microscopy (Müller-Reichert et al., 2007; Kukulski et al., 2011) can be used advantageously for imaging of proteins or organelles within cells because fluorescence microscopy allows specific molecular labeling and, in combination with new super-resolution fluorescence microscopy methods, spatial resolutions well below the diffraction barrier. Super-resolution fluorescence imaging by single-molecule photoactivation or photoswitching and position determination (localization microscopy) (Betzig et al., 2006; Hess et al., 2006; Rust et al., 2006; Heilemann et al., 2008; Sauer, 2013) can localize fluorescently labeled molecules at virtually molecular resolution. Furthermore, super-resolution fluorescence imaging enables higher labeling efficiencies than immunogold EM using fluorophore-tagged antibodies, which facilitates structure determination by localization microscopy. Thus, localization microscopy and EM are complementary methods that can be combined to determine molecular positions in the context of the cellular ultrastructure provided by EM with nanometer resolution (Betzig et al., 2006; Watanabe et al., 2011; Kopek et al., 2012; Nanguneri et al., 2012; Suleiman et al., 2013; Sochacki et al., 2014; Perkovic et al., 2014). In order to perform correlative localization and electron microscopy, several methodological requirements have to be fulfilled. First, protein fluorescence damage and autofluorescent background due to fixation and staining required to preserve good ultrastructure has to be kept to a minimum (Tsien, 1998; Watanabe et al., 2011). Second, protein positions determined by localization microscopy have to be located within the EM image across large areas with a precision in the nanometer range. This demand is impeded by a lack of suitable alignment markers that are stationary at the nanoscale range and exhibit good contrast in the two imaging modes (Watanabe et al., 2011; Kopek et al., 2012; Sochacki et al., 2014; Perkovic et al., 2014). Even when such types of markers are available, structural deformations occurring between the two imaging modes can aggravate the overlay of the two images with molecular precision.

Finally, one should bear in mind that localization microscopy can provide quantitative molecular information about molecular distributions and, appropriate controls assumed, absolute numbers of proteins present. Therefore, it has to be guaranteed that each protein of interest is labeled with an ‘active’ fluorophore and that its fluorescence is detected above a certain photon threshold (Sauer, 2013; Lando et al., 2012). This task is particularly demanding when using fluorophore-labeled antibodies for specific labeling.

Here, we demonstrate the use of correlative scanning electron (SEM) and direct stochastic optical reconstruction microscopy (dSTORM) (Heilemann et al., 2008; van de Linde et al., 2011;

¹Department of Biotechnology and Biophysics, Biozentrum, Julius Maximilian University Würzburg, Am Hubland, 97074 Würzburg, Germany. ²Department of Electron Microscopy, Biozentrum, Julius Maximilian University Würzburg, Am Hubland, 97074 Würzburg, Germany.

*Author for correspondence (m.sauer@uni-wuerzburg.de)

Received 15 May 2014; Accepted 6 August 2014

Löschberger et al., 2012) to image proteins of NPCs in isolated *Xenopus laevis* oocyte nuclear envelopes with molecular resolution in both imaging modes. Instead of using alignment markers, we use the periodic molecular structure of the NPC to localize proteins in *d*STORM and corresponding SEM images to overlay them with nanometer precision. Our results demonstrate quantitative molecular labeling of the NPC protein gp210 (also known as NUP210) (Favreau et al., 2001; Gerace et al., 1982; Gajewski et al., 1996) by standard immunocytochemistry with primary and secondary antibodies, and that the NPC contains eight gp210 homodimers. In addition, *d*STORM reveals subpopulations of NPCs with ninefold symmetry that are found occasionally among the more typical eightfold symmetrical structures (Hinshaw and Milligan, 2003).

RESULTS AND DISCUSSION

Recently, the NPC has been introduced as a suitable reference structure for verification of super-resolution imaging data. Two-color *d*STORM images recorded either consecutively or simultaneously by spectrally resolved imaging in combination with particle averaging demonstrated that the organization of NPC proteins can be visualized with nanometer resolution (Löschberger et al., 2012; Wolter et al., 2012). In order to shed light on the heterogeneity of NPC composition and quantify the labeling efficiency, we set out to localize the integral membrane protein gp210 (Favreau et al., 2001; Gerace et al., 1982) and *N*-acetylglucosamine-modified nucleoporins of the central channel of NPCs by correlative SEM and *d*STORM. Isolated *Xenopus laevis* oocyte nuclear envelopes were prepared on chambered cover glass without correlative markers (Fig. 1). The nuclear envelopes were labeled using a primary antibody directed against an epitope in the luminal side of gp210 (Gajewski et al., 1996), and Alexa Fluor 647 (Alexa 647)-labeled F(ab')₂ fragments or Alexa-647-labeled wheat germ agglutinin (WGA) binding to modified nucleoporins of the central channel (Davis and Blobel, 1987).

At this point, it has to be indicated that correlative imaging of NPCs in isolated nuclear envelopes with molecular resolution is

challenging because sample preparation generates a situation in which the cytoplasmic NPC side, with the anchoring proteins, is oriented in the direction of the coverglass, but SEM imaging is restricted to the nucleoplasmatic, nuclear-basket-containing side (Fig. 1A). Accidentally, we realized sample areas where the nuclear envelope folded back during preparation, hence, also enabling SEM of the cytoplasmic NPC side (Fig. 1B). However, it is impossible to identify such folded areas in fluorescence images. Therefore, in the majority of preparations the cytoplasmic side of the NPC is invisible in the SEM images. By contrast, the central channel and the integral membrane protein gp210 can be visualized from the cytoplasmic and nucleoplasmatic side by fluorescence imaging.

In localization microscopy, single-molecule coordinates are generally visualized as a histogram by using sub-pixel binning (Wolter et al., 2012; Wolter et al., 2010). To determine the influence of pixel binning on resolution, we reconstructed *d*STORM images of the central NPC channel at different pixel size (Fig. 1C). The resulting super-resolution images clearly demonstrate that the central channel of the NPC with a diameter of ~40 nm did not become visible until the pixel size was reduced below 20 nm. This finding demonstrates that we achieved a spatial resolution considerably better than 20 nm for imaging of the central channel in NPCs (Fig. 1C). The high spatial resolution is due to the large number of photons detected per Alexa 647, ~3,500 photons/frame, and the small size of a WGA dimer, of ~5 nm (Schwefel et al., 2010), used to label the nucleoporins of the central channel. In accordance with this finding, we determined a localization precision of ~6 nm (s.d., in the lateral direction) using localizations of unspecifically bound isolated WGA–Alexa-647 molecules in the sample.

Next, we mapped the *xy* positions of gp210 labeled with Alexa 647 antibody and WGA–Alexa-647-labeled nucleoporins onto the SEM image (Fig. 2). Image alignment was performed without markers, exploiting the highly symmetric circular structure of the NPC (supplementary material Figs S1, S2). The *xy* positions of Alexa 647 in the *d*STORM images matched the shapes of the

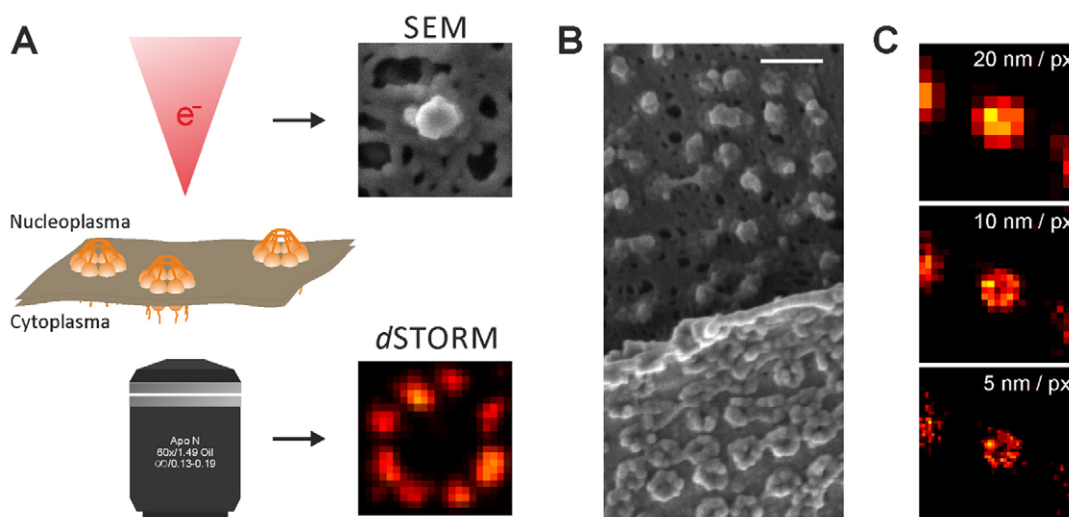


Fig. 1. Imaging the nuclear envelope by SEM and *d*STORM. (A) SEM imaging is restricted to the nucleoplasmatic, nuclear-basket-containing, side, whereas *d*STORM imaging is performed from the cytoplasmic side, where the anchoring proteins are oriented in the direction of the coverglass. Schematically, an electron beam and an objective are depicted to symbolize SEM and *d*STORM imaging, respectively. (B) SEM image of a folded nuclear envelope. (C) Influence of the pixel binning used to reconstruct the super-resolved *d*STORM image on resolution, that is, the visualization of the central channel of the NPC. Scale bar: 200 nm.

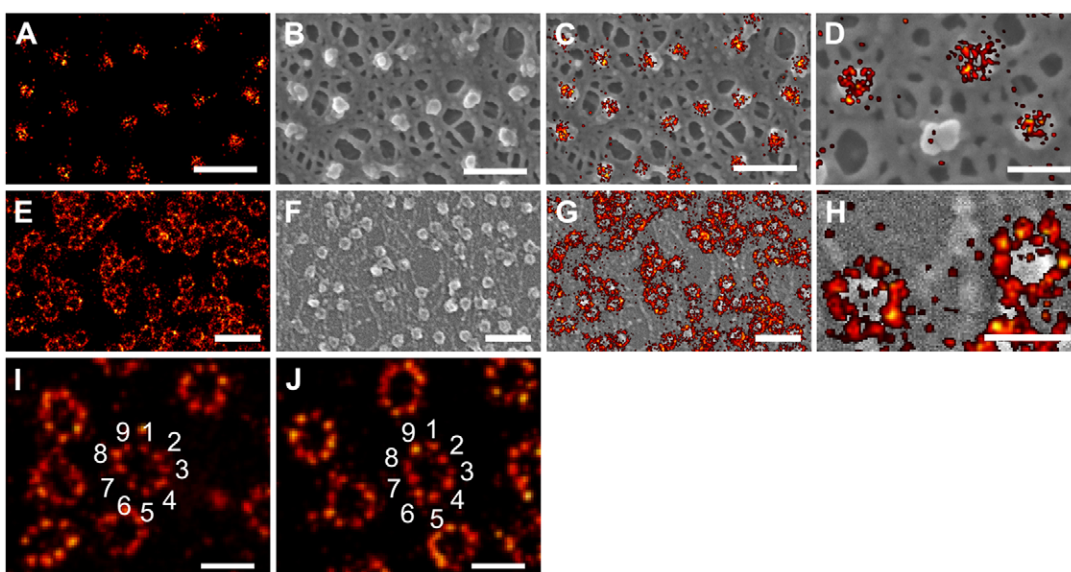


Fig. 2. Correlative dSTORM-SEM of NPCs. (A) dSTORM image of the central channel labeled with WGA–Alexa-647, (B) corresponding SEM image of the nucleoplasmic side of the nuclear envelope and (C) overlay of the dSTORM and SEM images. (D) Detailed overlay of a different area, highlighting that some NPCs are not labeled by WGA–Alexa-647. (E) The integral membrane protein gp210 was labeled using immunofluorescence with Alexa 647. (F) Corresponding SEM image, (G) overlay of dSTORM and SEM image and (H) overlay of the detailed eightfold structure of the outer gp210 ring. (I,J) Examples of NPCs revealing a ninefold symmetrical structure of gp210 proteins (Hinshaw and Milligan, 2003). Scale bars: 250 nm (A–C), 100 nm (D), 500 nm (E–G), 200 nm (H–J).

NPC structures in SEM (Fig. 2). The majority of WGA–Alexa-647-labeled NPCs showed the central channel perfectly superimposed with the SEM structures (Fig. 2A–D). Even in large correlative dSTORM-SEM images, the overlay error remained smaller than the spatial optical resolution (supplementary material Fig. S3).

By contrast, gp210 proteins were labeled by an antibody complex, which limited the overlay accuracy to ~ 20 nm. In addition, the dSTORM structures were generally larger than the corresponding SEM structures. However, because the overlay of the two images was not based on direct protein assignment but on the center of the NPC structures in dSTORM and SEM images, we also expect a smaller overlay error for the gp210 structure. Whether the simple overlay of the center of mass of localization microscopy and EM data also works for unsymmetrical structures needs to be tested.

The majority of gp210-labeled NPCs showed an eightfold symmetric arrangement surrounding the central channel (Fig. 2E–H). Some of the gp210 eightfold structures appeared slightly distorted, which arises from the spreading of the nuclear envelope on the coverglass. Only very rarely (<1%) could completely unlabeled NPCs be identified in dSTORM-SEM images (Fig. 2D). The same applies to the central channel labeled by WGA–Alexa-647. The infrequent appearance of completely unlabeled NPCs cannot be explained by labeling statistics but must be ascribed to incomplete compositions of NPCs or incomplete matured or erroneously folded proteins.

Interestingly, we also discovered some (<0.1%) NPCs featuring a ninefold rotational symmetry of gp210 proteins (Fig. 2I,J). Subpopulations of ninefold and tenfold symmetrical NPCs with slightly larger diameter have previously been found in preparations of *Xenopus oocyte* nuclei by EM, suggesting that the assembly process of NPCs can be influenced by local nuclear envelope inhomogeneity, e.g. curved membranes that favor the formation of larger NPCs due to packing constraints (Hinshaw and Milligan, 2003).

Taking advantage of the specific and efficient labeling properties of the anti-gp210 antibodies used (Gajewski et al., 1996) and the high detection and localization probability of Alexa 647, we set out to quantify the number of gp210 proteins surrounding the central channel of the NPC. So far, it is unclear whether eight or 16 gp210 proteins are arranged as monomers or homodimers around the central channel (Favreau et al., 2001; Gerace et al., 1982). Analysis of localization data of 318 NPCs revealed values of 274 ± 4 (mean \pm s.e.m.) localizations per NPC (median, 253) and 35.1 ± 0.5 (mean \pm s.e.m.) localizations per protein domain (median, 32) forming the eightfold NPC structure (Fig. 3A,B). This demonstrates that on average 7.9 domains are labeled and identified per NPC. For isolated fluorescence signals detected within the circular NPC structure, we determined a value of 8.1 ± 0.2 (mean \pm s.e.m.) localizations per Alexa-647-labeled F(ab')₂ fragment (median, 5.5) (Fig. 3C).

With the assumption that the isolated signals resulted from single Alexa-647-labeled F(ab')₂ fragments, we estimate that on average more than four Alexa-647-labeled F(ab')₂ fragments bind per gp210 domain. Given that the probability for binding of more than 4 F(ab')₂ fragments per primary antibody is negligibly low and it is known that the primary antibody X222 binds to a single epitope of the gp210 protein (Gajewski et al., 1996), our data provide evidence that each domain contains a gp210 homodimer labeled on average with two monoclonal X222 antibodies and four to six Alexa-647-labeled F(ab')₂ fragments. Control localization experiments with non-specifically adsorbed Alexa-647-labeled F(ab')₂ fragments on nuclear envelopes in the absence of the primary antibody directed against gp210 protein corroborated our finding that more than four Alexa-647-labeled F(ab')₂ fragments bound per gp210 domain (supplementary material Fig. S4).

To summarize, our data convincingly demonstrate that localization microscopy with standard fluorescent probes, such as fluorescently tagged antibodies, can map the position of

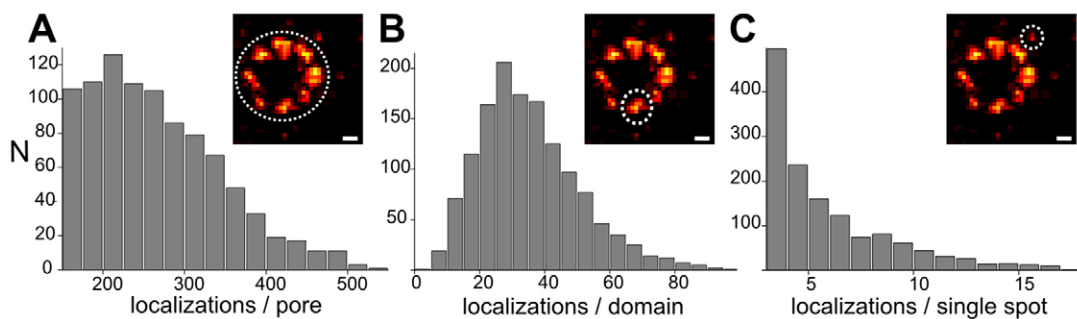


Fig. 3. Localization statistic of gp210 proteins labeled with a primary antibody and a secondary Alexa-647-labeled F(ab')₂ fragment. The mean localization number was determined as 274 ± 4 for whole NPCs (an example is shown in the inset) (A), 35.1 ± 0.5 for single domains (dashed ring in inset) within the eightfold NPC structure (B), and 8.1 ± 0.2 for isolated fluorescence signals (spots, dashed ring in inset) found in NPCs corresponding to an individual F(ab')₂ fragment (C) (mean \pm s.e.m.). Scale bars, 20 nm.

proteins in the context of the ultrastructure of large multiprotein complexes provided by EM with nanometer resolution and can reveal subpopulations with slightly altered characteristics that are washed out by particle averaging methods (Löschberger et al., 2012; Szymborska et al., 2013). In addition, correlative *d*STORM-SEM showed that NPCs were only rarely invisible in the fluorescence imaging mode but appear perfectly assembled in the EM imaging mode. These results emphasize the complementarity of the two imaging modes and also provide evidence for the reliability of *d*STORM when applied in combination with highly specific antibodies for quantitative super-resolution imaging. In combination with correlative focused ion beam scanning electron microscopy (FIB-SEM), *d*STORM can potentially be used also for 3D quantitative super-resolution imaging. Alternatively, the sample can be imaged with two-dimensional tiling and at multiple angles to create 3D tomograms in transmission electron microscopy (TEM) (Sochacki et al., 2014)

MATERIALS AND METHODS

Sample preparation for *d*STORM

Nuclear envelopes of *Xenopus laevis* oocytes were isolated as previously described (Löschberger et al., 2012). They were fixed for 20 min with 2% paraformaldehyde in phosphate-buffered saline (PBS). After a short washing step in PBS, they were saturated with 0.5% BSA (Serva) in PBS for 5 min. The envelopes were labeled with X222 antibodies (Gajewski et al., 1996) directed against gp210 for 45 min, washed for 10 min in PBS and incubated with Alexa-647-labeled F(ab')₂ fragments [Life Technologies, A-21237; degree of labeling (DOL) of ~ 3.5] of goat anti-mouse-IgG antibody for 30 min. Finally, a washing step of at least 20 min in PBS was performed. For WGA staining, the nuclear envelopes were incubated in 1 μ g/ml WGA-Alexa-647 (Sigma) in PBS for 10 min. Samples were stored in PBS with 0.2% sodium azide.

Localization microscopy

*d*STORM imaging was performed as described previously (van de Linde et al., 2011; Löschberger et al., 2012). Briefly, we used an inverted microscope (Olympus IX-71) equipped with an oil-immersion objective (APO N, $\times 60$, NA 1.49; Olympus). Irradiation at 640 nm was provided by a Genesis MX 639-1000 laser (Coherent). Typically, 20,000 frames were acquired with a frame rate of 105 Hz at excitation intensities of 1–10 kW cm⁻² using an inclined illumination scheme (van de Linde et al., 2011). *d*STORM images were reconstructed and analyzed with the open source software rapid*d*STORM 3.2 (Wolter et al., 2010; Wolter et al., 2012). Only fluorescent spots containing more than 1000 photons were analyzed. By analyzing their ellipticity, multi-fluorophore events were discarded from further analysis (Wolter et al., 2010; Wolter et al., 2012). Typically, 3500 photons were detected per Alexa 647 molecule and

frame. Localizations of 845 unspecifically bound, isolated WGA-Alexa-647 molecules were aligned to their center of mass and binned into one histogram. The localization precision (s.d.) was determined as 6.41 ± 0.03 nm (s.e.m. of data fit) by fitting a two-dimensional Gaussian function to the data.

Scanning electron microscopy

After finishing the *d*STORM analysis, nuclear envelopes were fixed for 24 h at 4°C with 2.5% glutaraldehyde (50 mM sodium cacodylate pH 7.2, 50 mM KCl, 2.5 mM MgCl₂) and washed three times each for 3 min with 50 mM sodium cacodylate (pH 7.2). Specimens were then fixed for 2 h at 4°C with 2% OsO₄ buffered with 50 mM sodium cacodylate (pH 7.2), washed with distilled H₂O, dehydrated stepwise with acetone and dried using a critical point dryer (CPD 030; BAL-TEC, Liechtenstein). Dried specimens were carbon coated (MED 010 BAL-TEC, Liechtenstein) and analyzed with a JEOL field emission scanning electron microscope (JSM-7500F) at 1 kV using the modus gentle beam high at a working distance of 4.5–5 mm. Overview images were used to recognize the previously super-resolved areas (supplementary material Fig. S3).

Image alignment

Thanks to their highly symmetrical structure, NPCs can be used for intrinsic image alignment. The center of the gp210 or WGA ring structure in *d*STORM and SEM images that matched were identified manually (supplementary material Fig. S4) and used as reference points (landmarks). bUnwarpJ was used for image registration (Arganda-Carreras et al., 2006). Typically, six landmarks in different parts of the *d*STORM and SEM images were used for transformation of a 2.5×2.5 μ m² image area. Briefly, bUnwarpJ calculates a B-spline transformation for registering two images. GIMP 2.8.10 was used to make the *d*STORM images transparent before correlative overlay with the SEM images.

Quantification of *d*STORM data

First, single NPCs were separated by applying a canny edge filter to the *d*STORM image. The vertices of the resulting mask were used to crop localization sets of single NPCs from the data provided by rapid*d*STORM (Wolter et al., 2010; Wolter et al., 2012). To allocate the whole NPC into single gp210 domains, a multilevel *k*-means algorithm was applied to the localization cloud. Using the known spatial features of the gp210 ring (i.e. the existence of a maximum of eight separated domains and their circular symmetry), starting points for the *k*-means clustering can be provided, minimizing the usual difficulties with *k*-means clustering. First, a mean component analysis (MCA) was performed on the *x* and *y* coordinates of all localizations of the single NPC candidate. NPCs exhibiting a ratio of the absolute values of the resulting eigenvectors larger than two were discarded to exclude overlapping pores and other artifacts from the canny edge filter. Afterwards an ellipse was fitted to the

localization ring, again using the eigenvectors resulting from the MCA. Starting points were then set by distributing the intended number of domains, N , randomly but (angularly) equidistant along the ellipse. It appeared that lower starting values than five domains were not necessary. A second set of starting points was generated by turning the first set by $N^{-1} \times \alpha$, where α is the angle between two neighboring domains. This procedure is repeated for $N \times [5, 6, 7, 8]$. Subsequently each candidate domain in the current subset was subjected to an Anderson–Darling test (Hamerly and Elkan, 2004) to evaluate whether the current separation was sufficient or not. Briefly, every candidate domain was tested for whether their spatial localization distribution in x and y , respectively, is Gaussian like. If this is not the case for at least one candidate, the current separation state is rejected, and the next parameter set is tried. If there is no successful test for the last parameter set, which is usually the ‘eight turned starting points’ configuration, the candidate is discarded. This might be the case for candidates that were cropped faulty from the canny edge detector or had insufficient spatial resolution, causing the domains to overlap significantly. Both cases were very rarely apparent. All further analyzing steps following the separation process, for example, production of histograms and localization counts, were conducted directly by additional PYTHON scripts or in OriginPro 8.5 (OriginLab).

Acknowledgements

We thank Christian Stigloher and Thomas Niehörster for help with sample preparation and discussion.

Competing interests

The authors declare no competing interests.

Author contributions

A.L., G.K., S.v.d.L., C.F. and M.S. conceived of and designed the experiments; A.L. and G.K. performed the experiments; C.F. and S.v.d.L. analyzed the data; M.S. wrote the paper.

Funding

This work was supported by the Biophotonics Initiative of the Bundesministerium für Bildung und Forschung [grant numbers 13N11019 and 13N12781].

Supplementary material

Supplementary material available online at
<http://jcs.biologists.org/lookup/suppl/doi:10.1242/jcs.156620/-/DC1>

References

- Arganda-Carreras, C., Sánchez Sorzano, Ó., Marabini, R., Carazo, J. M., Ortiz-de Solorzano, C. and Kybic, J. (2006). Consistent and elastic registration of histological sections using vector-spline regularization. *Computer Vision Approaches to Medical Image Analysis* **4241**, 85–95.
- Beck, M., Lucić, V., Förster, F., Baumeister, W. and Medalia, O. (2007). Snapshots of nuclear pore complexes in action captured by cryo-electron tomography. *Nature* **449**, 611–615.
- Betzig, E., Patterson, G. H., Sougrat, R., Lindwasser, O. W., Olenych, S., Bonifacino, J. S., Davidson, M. W., Lippincott-Schwartz, J. and Hess, H. F. (2006). Imaging intracellular fluorescent proteins at nanometer resolution. *Science* **313**, 1642–1645.
- Davis, L. I. and Blobel, G. (1987). Nuclear pore complex contains a family of glycoproteins that includes p62: glycosylation through a previously unidentified cellular pathway. *Proc. Natl. Acad. Sci. USA* **84**, 7552–7556.
- Favreau, C., Bastos, R., Cartaud, J., Courvalin, J. C. and Mustonen, P. (2001). Biochemical characterization of nuclear pore complex protein gp210 oligomers. *Eur. J. Biochem.* **268**, 3883–3889.
- Gajewski, A., Lourim, D. and Krohne, G. (1996). An antibody against a glycosylated integral membrane protein of the Xenopus laevis nuclear pore complex: a tool for the study of pore complex membranes. *Eur. J. Cell Biol.* **71**, 14–21.
- Gerace, L., Ottaviano, Y. and Kondor-Koch, C. (1982). Identification of a major polypeptide of the nuclear pore complex. *J. Cell Biol.* **95**, 826–837.
- Hamerly, G. and Elkan, C. (2004). Learning the k in k -means. *Adv. Neural Inf. Process. Syst.* **16**, 281–288.
- Heilemann, M., van de Linde, S., Schüttelpehl, M., Kasper, R., Seefeldt, B., Mukherjee, A., Tinnefeld, P. and Sauer, M. (2008). Subdiffraction-resolution fluorescence imaging with conventional fluorescent probes. *Angew. Chem. Int. Ed. Engl.* **47**, 6172–6176.
- Hess, S. T., Girirajan, T. P. and Mason, M. D. (2006). Ultra-high resolution imaging by fluorescence photoactivation localization microscopy. *Biophys. J.* **91**, 4258–4272.
- Hinshaw, J. E. and Milligan, R. A. (2003). Nuclear pore complexes exceeding eightfold rotational symmetry. *J. Struct. Biol.* **141**, 259–268.
- Kopek, B. G., Shtengel, G., Xu, C. S., Clayton, D. A. and Hess, H. F. (2012). Correlative 3D superresolution fluorescence and electron microscopy reveal the relationship of mitochondrial nucleoids to membranes. *Proc. Natl. Acad. Sci. USA* **109**, 6136–6141.
- Kukulski, W., Schorb, M., Welsch, S., Picco, A., Kaksonen, M. and Briggs, J. A. G. (2011). Correlated fluorescence and 3D electron microscopy with high sensitivity and spatial precision. *J. Cell Biol.* **192**, 111–119.
- Lando, D., Endesfelder, U., Berger, H., Subramanian, L., Dunne, P. D., McColl, J., Klenerman, D., Carr, A. M., Sauer, M., Allshire, R. C. et al. (2012). Quantitative single-molecule microscopy reveals that CENP-A(Cnp1) deposition occurs during G2 in fission yeast. *Open Biol.* **2**, 120078.
- Löschberger, A., van de Linde, S., Dabauvalle, M. C., Rieger, B., Heilemann, M., Krohne, G. and Sauer, M. (2012). Super-resolution imaging visualizes the eightfold symmetry of gp210 proteins around the nuclear pore complex and resolves the central channel with nanometer resolution. *J. Cell Sci.* **125**, 570–575.
- Maimon, T., Elad, N., Dahan, I. and Medalia, O. (2012). The human nuclear pore complex as revealed by cryo-electron tomography. *Structure* **20**, 998–1006.
- Morphew, M. K. (2007). 3D immunolocalization with plastic sections. *Methods Cell Biol.* **79**, 493–513.
- Müller-Reichert, T., Srayko, M., Hyman, A., O'Toole, E. T. and McDonald, K. (2007). Correlative light and electron microscopy of early *Caenorhabditis elegans* embryos in mitosis. *Methods Cell Biol.* **79**, 101–119.
- Nanguneri, S., Flotmann, B., Horstmann, H., Heilemann, M. and Kuner, T. (2012). Three-dimensional, tomographic super-resolution fluorescence imaging of serially sectioned thick samples. *PLoS ONE* **7**, e38098.
- Perkovic, M., Kunz, M., Endesfelder, U., Bunse, S., Wigge, C., Yu, Z., Hodirnau, V.-V., Scheffer, M. P., Seybert, A., Malkusch, S. et al. (2014). Correlative light- and electron microscopy with chemical tags. *J. Struct. Biol.* **186**, 205–213.
- Rust, M. J., Bates, M. and Zhuang, X. (2006). Sub-diffraction-limit imaging by stochastic optical reconstruction microscopy (STORM). *Nat. Methods* **3**, 793–796.
- Sauer, M. (2013). Localization microscopy coming of age: from concepts to biological impact. *J. Cell Sci.* **126**, 3505–3513.
- Schwefel, D., Maierhofer, C., Beck, J. G., Seeberger, S., Diederichs, K., Möller, H. M., Welte, W. and Wittmann, V. (2010). Structural basis of multivalent binding to wheat germ agglutinin. *J. Am. Chem. Soc.* **132**, 8704–8719.
- Sochacki, K. A., Shtengel, G., van Engelenburg, S. B., Hess, H. F. and Taraska, J. W. (2014). Correlative super-resolution fluorescence and metal-replica transmission electron microscopy. *Nat. Methods* **11**, 305–308.
- Suleiman, H., Zhang, L., Roth, R., Heuser, J. E., Miner, J. H., Shaw, A. S. and Dani, A. (2013). Nanoscale protein architecture of the kidney glomerular basement membrane. *eLife* **2**, e01149.
- Szymorska, A., de Marco, A., Daigle, N., Cordes, V. C., Briggs, J. A. G. and Ellenberg, J. (2013). Nuclear pore scaffold structure analyzed by super-resolution microscopy and particle averaging. *Science* **341**, 655–658.
- Tsien, R. Y. (1998). The green fluorescent protein. *Annu. Rev. Biochem.* **67**, 509–544.
- van de Linde, S., Löschberger, A., Klein, T., Heidbreder, M., Wolter, S., Heilemann, M. and Sauer, M. (2011). Direct stochastic optical reconstruction microscopy with standard fluorescent probes. *Nat. Protoc.* **6**, 991–1009.
- Watanabe, S., Punge, A., Hollopeter, G., Willig, K. I., Hobson, R. J., Davis, M. W., Hell, S. W. and Jorgensen, E. M. (2011). Protein localization in electron micrographs using fluorescence nanoscopy. *Nat. Methods* **8**, 80–84.
- Wolter, S., Schüttelpehl, M., Tscherpanow, M., VAN DE Linde, S., Heilemann, M. and Sauer, M. (2010). Real-time computation of subdiffraction-resolution fluorescence images. *J. Microsc.* **237**, 12–22.
- Wolter, S., Löschberger, A., Holm, T., Aufmkolk, S., Dabauvalle, M.-C., van de Linde, S. and Sauer, M. (2012). rapidSTORM: accurate, fast open-source software for localization microscopy. *Nat. Methods* **9**, 1040–1041.

Supplementary Material

Correlative super-resolution fluorescence and scanning electron microscopy of the nuclear pore complex with molecular resolution

Anna Löschberger¹, Christian Franke¹, Georg Krohne²,
Sebastian van de Linde¹, and Markus Sauer¹

¹Department of Biotechnology and Biophysics, Biozentrum
Julius Maximilian University Würzburg
Am Hubland
97074 Würzburg
Germany

²Department of Electron Microscopy, Biozentrum
Julius Maximilian University Würzburg,
Am Hubland, 97074 Würzburg,
Germany

Email: m.sauer@uni-wuerzburg.de

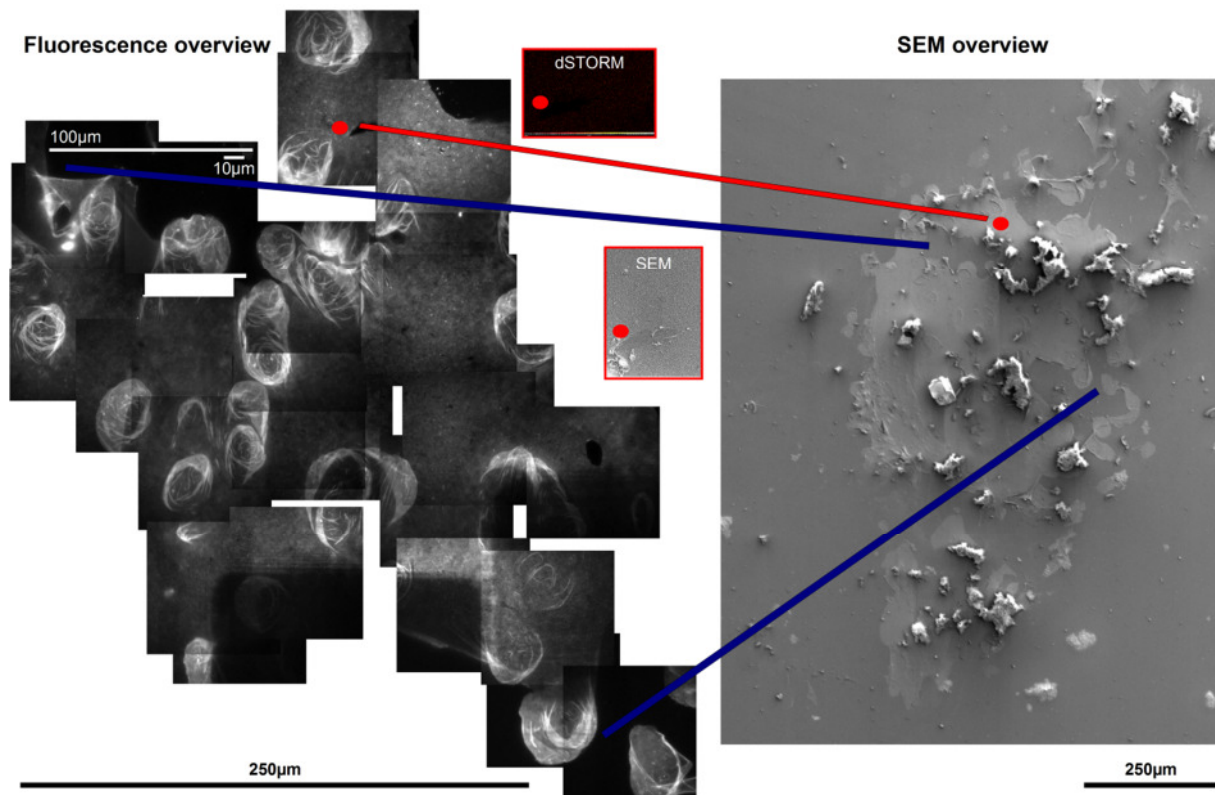


Figure S1. Correlative imaging procedure. Wide-field fluorescence and SEM overviews of nuclear envelopes of *Xenopus laevis* oocytes were used to find the region of interest (red dot) for SEM after dSTORM imaging. Blue and red lines serve as orientation. Scale bars, see image.

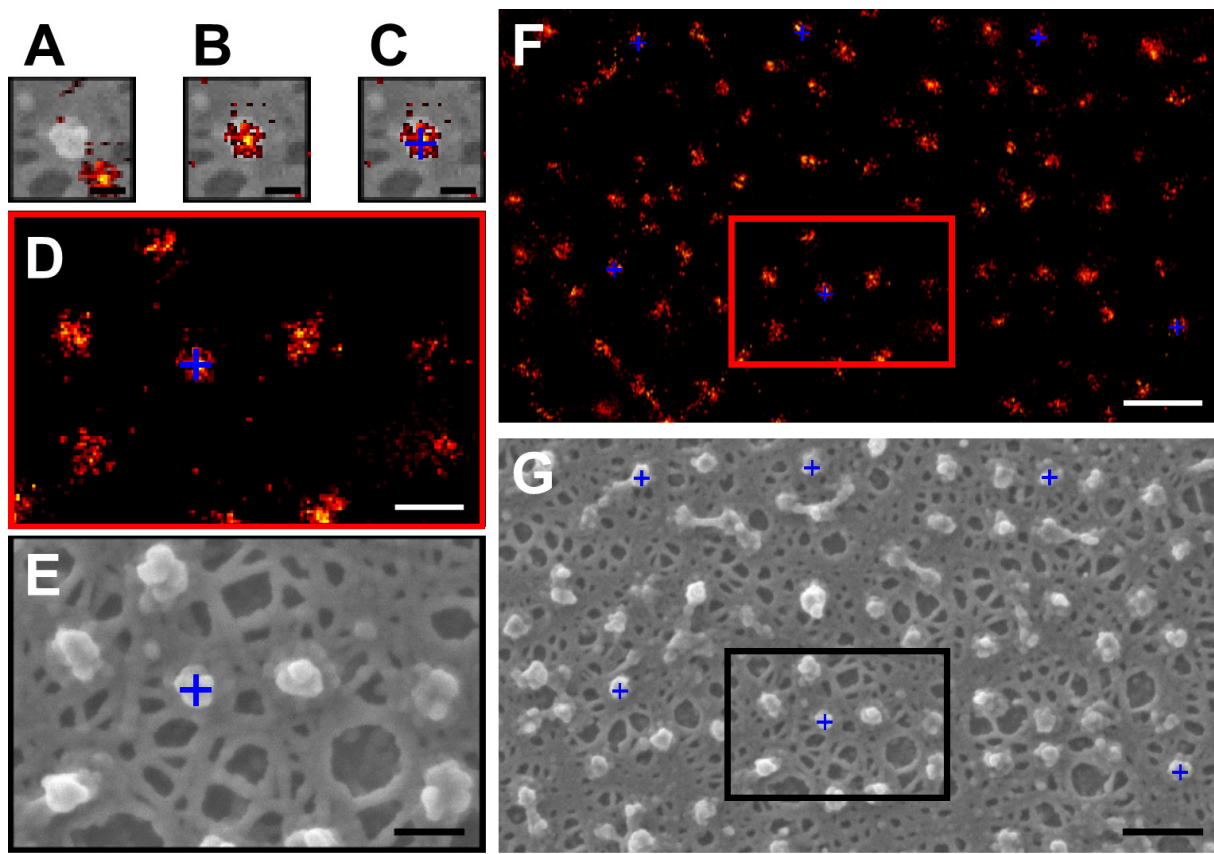


Figure S2. Landmark selection for correlative images of WGA Alexa Fluor 647 labeled NPCs of *Xenopus laevis* oocytes. (A-G) After adjusting the pixel size of the dSTORM and the SEM image the dSTORM/SEM overlay image is moved manually to a corresponding SEM pore (A,B). Corresponding pores are landmarked (+) (C-E). Only nuclear pores that match each other very precisely are chosen for future landmarks (F,G). Images were finally transformed with bUnwarpJ. Scale bars, 50 nm (A-C), 100 nm (D,E), 250 nm (F,G).

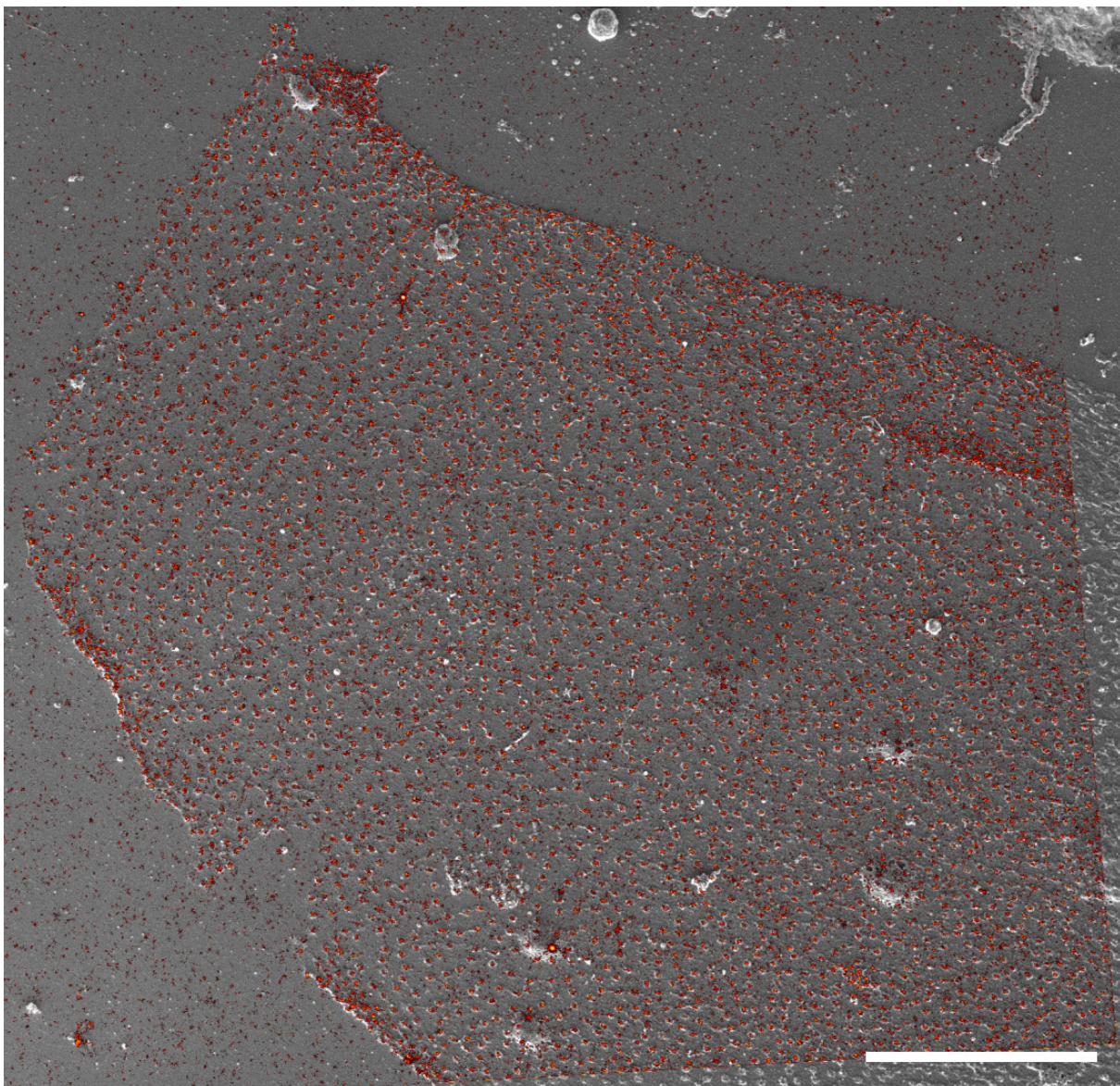


Figure S3. Correlative SEM-dSTORM image. The majority of Alexa 647 WGA labeled NPCs perfectly fit the SEM image. Scale bar, 5 μ m.

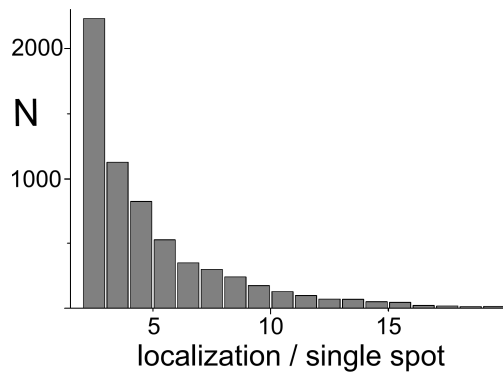


Figure S4. Localization statistics of Alexa 647 labeled F(ab')₂ fragments in the absence of primary antibody directed against gp210 proteins. Single-molecule experiments (sample size 5.000 isolated fluorescence signals) with Alexa 647 labeled F(ab')₂ fragments non-specifically adsorbed on nuclear envelopes show a similar distribution of localizations identified per single spatially isolated fluorescence signal than obtained in our quantification experiments (Fig. 3C). The mean localization number is determined to 5.4 ± 0.1 (s.e.) localizations per Alexa 647 labeled F(ab')₂ fragment (median: 3.5).